Feedback and the Structure of Simulated Galaxies at redshift z=2

Laura V. Sales[1], Julio F. Navarro[2,3]⋆, Joop Schaye[4], Claudio Dalla Vecchia[4,5], Volker Springel[6,7,8] and C. M. Booth[4]

[1] *Kapteyn Astronomical Institute, P.O. Box 800, Groningen, The Netherlands*
[2] *Department of Physics and Astronomy, University of Victoria, Victoria, BC V8P 5C2, Canada*
[3] *Department of Astronomy, University of Massachusetts, US*
[4] *Leiden Observatory, Leiden University, PO Box 9513, 2300 RA Leiden, The Netherlands*
[5] *Max-Planck-Institute for Extraterrestrische Physik, Giessenbachstrasse, D-85478, Garching, Germany*
[6] *Max Planck Institute for Astrophysics, Karl-Schwarzschild-Strasse 1, 85740 Garching, Germany*
[7] *Heidelberg Institute for Theoretical Studies, Schloss-Wolfsbrunnenweg 35, 69118 Heidelberg, Germany*
[8] *Zentrum für Astronomie der Universitä Heidelberg, Mönchhofstr. 1214, 69120 Heidelberg, Germany*

3 May 2010

ABSTRACT

We study the properties of simulated high-redshift galaxies using cosmological N-body/gasdynamical runs from the OverWhelmingly Large Simulations (OWLS) project. The runs contrast several feedback implementations of varying effectiveness: from no-feedback, to supernova-driven winds to powerful AGN-driven outflows. These different feedback models result in large variations in the abundance and structural properties of bright galaxies at $z = 2$. In agreement with earlier work, models with inefficient or no feedback lead to the formation of massive compact galaxies collecting a large fraction (upwards of 50%) of all available baryons in each halo. Increasing the efficiency of feedback reduces the baryonic mass and increases the size of simulated galaxies. A model that includes supernova-driven gas outflows aided by the energetic output of AGNs reduces galaxy masses by roughly a factor of ~ 10 compared with the no-feedback case. Other models give results that straddle these two extremes. Despite the large differences in galaxy formation efficiency, the net specific angular momentum of a galaxy is, on average, roughly half that of its surrounding halo, independent of halo mass (in the range probed) and of the feedback scheme. Feedback thus affects the baryonic mass of a galaxy much more severely than its spin. Feedback induces strong correlations between angular momentum content and galaxy mass that leave their imprint on galaxy scaling relations and morphologies. Encouragingly, we find that galaxy disks are common in moderate-feedback runs, making up typically $\sim 50\%$ of all galaxies at the centers of haloes with virial mass exceeding $\sim 10^{11} \, M_{\odot}$. The size, stellar masses, and circular speeds of simulated galaxies formed in such runs have properties in between those of large star-forming disks and of compact early-type galaxies at $z = 2$. Once the detailed abundance and structural properties of these rare objects are well established it may be possible to use them to gauge the overall efficacy of feedback in the formation of high redshift galaxies.

Key words: galaxies: haloes - galaxies: formation - galaxies: evolution - galaxies: kinematics and dynamics.

1 INTRODUCTION

The established paradigm for structure formation offers a clear road map for galaxy formation. Primordial fluctuations in the dominant cold dark matter (CDM) component of the Universe grow via gravitational instability, sweeping baryons into an evolving hierarchy of dark matter haloes that grow through mergers of preexisting units as well as through the accretion of material from the intergalactic medium (White & Rees 1978). On galaxy mass scales, baryons caught in a halo are able to radiate away the gravitational energy gained through the collapse, sink to the center of the halo, and assemble into the dense aggregations of gas and stars that we call galaxies (Blumenthal et al. 1985).

The structure and morphology of a galaxy results from the complex interplay between the time of collapse, the mode of assembly, the efficiency of cooling, and the rate of transformation of

⋆ Fellow of the Canadian Institute for Advanced Research.

gas into stars (see, e.g., Steinmetz & Navarro 2002). Where cooling dominates and outpaces star formation, baryons collect into thin, rotationally-supported disks (Fall & Efstathiou 1980). Stars formed in these disks inherit these morphological features, but are vulnerable to swift transformation into dispersion-supported spheroids during subsequent merger events (Toomre 1977). Disks may re-form if mergers or accretion bring fresh supplies of cooled gas, making morphology a constantly evolving rather than an abiding feature of a galaxy (Cole et al. 2000; Robertson et al. 2006).

The galaxy formation scenario driven by gravitational collapse and radiative losses outlined above is compelling, but incomplete. Indeed, cooling is so effective at early times that, unless impeded somehow, most baryons would be turned into stars in early-collapsing protogalaxies, which would then merge away to form by the present time a majority of spheroid-dominated remnants, in vehement disagreement with observations (White & Rees 1978; Cole 1991; White & Frenk 1991). The problem is compounded by the fact that, during mergers, cooled gas tends to transfer its angular momentum to the surrounding dark matter halo. As a result, even in cases where disks could form, their structural properties would be at odds with those of spiral galaxies (Navarro & Benz 1991; Navarro et al. 1995; Navarro & Steinmetz 1997).

A gas heating mechanism that prevents runaway cooling and that regulates the formation of stars in step with mergers and accretion is widely believed to be the most likely solution to these problems. The energetic output from evolving stars and supernovae is a natural candidate. It scales directly with star formation and, in a typical galaxy, the total energy released by supernovae can be comparable to the binding energy of the baryons. Thus, if channeled properly, feedback energy from supernovae may temper the gravitational deposition of cooled gas into a galaxy and effectively self-regulate its star formation history (White & Frenk 1991).

The even standing of gravity, feedback and cooling may thus help reconcile the observed galaxy population with hierarchical clustering models, but it comes at the price of complexity: the main structural properties of a galaxy, such as stellar mass, rotation speed, and morphology, are then expected to depend on details of its assembly history, such as the exact timing, geometry and mass spectrum of accretion events (see, e.g., Abadi et al. 2003a,b; Meza et al. 2003; Governato et al. 2007; Zavala et al. 2008; Scannapieco et al. 2009; Governato et al. 2010).

Such sensitivity to feedback has held back progress in direct simulation of the process of galaxy formation. As recent work demonstrates, different but plausible implementations of feedback within the *same* dark halo lead to galaxies of very different mass, morphology, dynamics, and star formation history (see, e.g., Okamoto et al. 2005). Numerical parameters may thus be tuned to reproduce some properties of individual galaxies, but at the expense of wider predictability in the modeling.

These results suggest that further progress in the subject requires the testing of different feedback schemes on a statistically significant sample of dark haloes formed with representative assembly histories. The viability of each feedback implementation may then be assessed by contrasting the statistics of such samples with observational constraints such as the stellar mass function, clustering, color distribution, and scaling laws.

We take a step in this direction here by analyzing a subset of cosmological N-body/gasdynamical simulations from the OverWhelmingly Large Simulations (OWLS) project (Schaye et al. 2010). We present results regarding the morphology, stellar mass, and angular momentum content of galaxies assembled at $z = 2$, and compare them with the few observational constraints available

at that epoch. We limit our analysis to the $z = 2$ galaxy population because most high-resolution OWLS runs follow volumes too small to be evolved until $z = 0$. In future papers, we plan to extend this analysis to the present-day galaxy population using samples drawn from the closely-related GIMIC project, designed to follow a few representative volumes selected from the Millennium Simulation (Crain et al. 2009).

The paper is organized as follows. In Sec. 2 we present a short overview of the simulations and feedback models. We then present our main numerical results in Sec. 3 and analyze them in the context of available observational constraints in Sec. 4. We end with a brief summary in Sec. 5.

2   THE NUMERICAL SIMULATIONS

2.1   The OWLS runs

The OWLS project consists of a suite of ~ 50 different cosmological N-body/SPH simulations that follow the evolution of dark matter and baryons in boxes of 25 and 100 h^{-1} Mpc (comoving). Each box is run many times, varying the numerical implementation of various aspects of the gas cooling, star formation and feedback modules (see Schaye et al. 2010, for further details).

We have selected for our analysis nine 25 h^{-1} Mpc-box OWLS runs, eight of which explore different feedback implementations with 512^3 dark matter and 512^3 baryonic particles whilst keeping other subgrid parameters constant, such as the stellar initial mass function (IMF), the star formation threshold and its efficiency. The ninth repeats one of the runs, at $8\times$ lower mass resolution (and $2\times$ lower spatial resolution), in order to provide some guidance regarding the sensitivity of our results to numerical resolution.

All simulations assume a standard WMAP-3 ΛCDM cosmogony, start at $z_i = 127$ and, because of their small box size, they have only been carried out to $z = 2$. We adopt this cosmology for all physical quantities listed here. We make explicit the dependence on the Hubble constant, h, for simulation parameters, but drop the h dependence and adopt $h = 0.73$ when comparing with observations.

The high-resolution runs have a comoving gravitational softening lengthscale of 1/25 of the initial mean inter-particle spacing at high redshift. These are switched later to a fixed physical value so that the softening never exceeds $0.5 h^{-1}$ kpc (physical). The mass per baryonic particle is $\sim 1.4 \times 10^6 h^{-1} M_\odot$ and 4.5 times higher for the dark matter component. All runs assume that the Universe is reionized at $z = 9$ (for H) and at $z = 3.5$ (He) by a bath of energetic photons whose properties evolve as proposed by Haardt & Madau (2001).

Table 1 summarizes the most important numerical parameters of the simulations, as well as the cosmological parameters.

2.2   Subgrid gas physics

Baryons are assumed to trace the dark matter distribution at the initial redshift. Whilst in gaseous form, they are followed hydrodynamically and are subject to pressure gradients and shocks. Radiative cooling and heating is implemented following Wiersma et al. (2009a), which also accounts for the photo-ionisation of metals due to the UV background.

In collapsed structures, gas can cool and sink to the center of these haloes, where it may reach high overdensities before

Table 1. Simulation parameters

Ω_{M}	0.238
Ω_{CDM}	0.1962
Ω_b	0.0418
Ω_{Λ}	0.762
σ_8	0.74
h	0.73
n	0.951
Reionization redshift	9 (H), 3.5 (He)
Mass per DM particle	$m_p = 6.3 \times 10^6 h^{-1} \mathrm{M}_\odot$
Mass per baryonic particle	$m_p = 1.4 \times 10^6 h^{-1} \mathrm{M}_\odot$
Number of particles	2×512^3
Box size	$25\, h^{-1}\,\mathrm{Mpc}$

turning into stars. With limited numbers of particles, these regions are poorly resolved and vulnerable to numerical instabilities, such as artificial clumping and fragmentation. As discussed by Springel & Hernquist (2003), these shortcomings can be alleviated by adopting, in high-density regions, a multi-phase description for the gas where the effective equation of state differs from the simple ideal gas law. In practice, we impose a polytropic equation of state (PEOS; $P \propto \rho^\gamma$, with $\gamma = 4/3$) on all gas particles whose density exceeds a critical value of $n_c = 0.1$ cm^{-3}, the density above which the gas is expected to be multiphase and unstable to star formation (Schaye 2004). This choice ensures that the Jeans mass in high-density regions is independent of ρ, effectively suppressing artificial clumping and reducing the dependence of star formation algorithms on numerical resolution (Schaye & Dalla Vecchia 2008).

2.3 Star formation algorithm

Star formation is implemented as described in detail by Schaye & Dalla Vecchia (2008). In brief, stars form out of PEOS gas particles with pressure-dependent parameters chosen to reproduce a Kennicutt-Schmidt law with index 1.4 (Kennicutt 1998). We assume a Chabrier initial mass function (Chabrier 2003) in order to take into account the enrichment and energy injected into the surroundings of young star particles by the explosion of SNII and SNIa supernovae. The energy per supernova explosion is chosen to be 10^{51} ergs. These events, together with mass loss from intermediate mass stars, pollute neighboring gas particles with metals, as described in Wiersma et al. (2009b). We track 11 species and include them in the computation of the cooling function, as in Wiersma et al. (2009a).

2.4 Feedback Models

The runs we analyze here explore alternative feedback implementations where the total amount of energy injected by supernovae into the surrounding ISM is kept constant, but the numerical algorithm used to inject this energy is varied. All runs that include feedback from core collapse supernova feedback assume a total energy input of 10^{51} ergs per solar mass of stars formed, 40% of which is invested into driving outflowing winds. The remainder is assumed to be lost to radiative processes.

2.4.1 Thermal Feedback

The simplest possibility, which we label "thermal feedback" (ThF), is to use the supernova energy to raise the internal energy of the surrounding gas particles. As reported in earlier work (Katz 1992), these regions typically have such short cooling times that the injected energy is quickly radiated away, with little hydrodynamical effect on the surrounding gas. As a result, thermal feedback is rather inefficient, and has little effect in regulating gas cooling and star formation, even though the implementation here follows the stochastic heating method described in Schaye et al. (2010) and presented in more detail in Dalla Vecchia et al. (in preparation), which is more resilient to numerical resolution limitations than the implementations adopted in earlier work (see also Kay et al. 2003).

2.4.2 Kinetic Feedback

A second possibility is to invest part of the feedback energy directly into gas bulk motions, with the aim of allowing gas to outflow from regions of active star formation, thus increasing the overall efficiency of feedback. These wind models are characterized by a couple of parameters: a "mass loading" factor, η, specifying the number of gas particles amongst which the injected energy is shared, and a "wind velocity", v_{w}, characterizing the kinetic energy of the outflow. For given energy, η and v_{w} are related by a constant $\eta \, v_{\mathrm{w}}^2$.

Our runs test three different possibilities for η: 1, 2 and 4, and their respective v_{w}, as summarized in Table 2. We refer to these runs as WF1, WF2, and WF4, respectively. WF2LR is equivalent to WF2 but run at $8\times$ poorer mass resolution and $2\times$ poorer spatial resolution.

As discussed by Springel & Hernquist (2003), a possible modification that can enhance feedback efficiency is to temporarily "decouple" the wind particle(s) hydrodynamically from the surrounding ISM. This facilitates large-scale galactic outflows and regulates star formation more effectively by enhancing the removal of gas from active star-forming regions (see e.g., Dalla Vecchia & Schaye 2008). We label this run WF2Dec.

A further run probes the possibility that the efficiency of feedback should correlate with the local density of the gas. We explore a model in which the wind velocity and mass loading are related to the gas density by $v_{\mathrm{w}} \propto \rho^{1/6}$ and $\eta \propto \rho^{-1/3}$. This guarantees that the wind velocity scales with the local gas sound speed ($v_{\mathrm{w}} \propto c_s$) given the aforementioned effective PEOS that holds in star-forming regions. The v_{w} and η relations are normalized so that, at the gas density corresponding to the star formation threshold ($n_c = 0.1$ cm^{-3}), they match $v_{\mathrm{w}} = 600$ km/s and $\eta = 2$ particles, consistent with the WF2 run. We will refer to this run as WDENS.

2.4.3 AGN Feedback

Our next model enhances feedback by adding to the WF2 feedback the extra energetic input from AGN. This model, which we refer to as AGN, for short, follows the numerical procedure introduced by Booth & Schaye (2009) and summarized in Schaye et al. (2010). Seed black holes with mass $m_{\mathrm{seed}} = 9 \times 10^4 \, M_\odot$ are placed at the center of all haloes that exceed a threshold virial mass of $4 \times 10^{10} h^{-1} M_\odot$. BHs can then grow by mass accretion and mergers with other BHs. A fraction ϵ_f of the total radiated energy due to the mass accretion onto the BHs is assumed to couple to the surrounding ISM. This efficiency is set to $\epsilon_f = 0.15$ to match local constraints on the number density as well as relations between

Table 2. Parameters of the different feedback models probed in each run. First and second columns list the short name (used throughout this paper) and the name originally used in Schaye et al. (2010), respectively. The third and fourth columns list the mass loading (η) and wind velocity (v_w) parameters of each model. The WF2Dec is the only model where wind gas particles are temporarily kinematically decoupled from the surrounding gas. This aids the removal of gas from galaxies and results in increased feedback efficiency. The characteristic density n_w used for scaling the WDENS wind parameters is that corresponding to the star formation threshold: $n_c = 0.1$ cm^{-3}.

Short name	OWLS name	η [particles]	v_w [km/s]
NoF	NOSN_NOZCOOL	–	–
ThF	WTHERMAL	–	–
WF4	WML4V424	4	424
WF2	REF	2	600
WF1	WML1V848	1	848
WF2Dec	WHYDRODEC	2	600
WDENS	WDENS	$2(n/n_\mathrm{w})^{-1/3}$	$600(n/n_\mathrm{w})^{1/6}$
AGN	AGN	2	600

BHs and host galaxy properties, both at redshift zero. AGN feedback is implemented as a *thermal* injection of energy (as opposed to the kinetic prescription used to model the stellar feedback), in the way described in Booth & Schaye (2009). Because it combines the supernova and AGN energetic outputs, the AGN run is the most effective feedback model tried in our series.

2.4.4   No Feedback

Finally, mainly for comparison purposes we also analyze a run that follows star formation like in the other implementations but neglects all energy injection into the ISM due to either supernovae or AGN. Gas cooling in this "no feedback" model, NoF, adopts the cooling function of a gas with primordial abundances, but in the absence of feedback this is only a minor difference that has little impact on the results. The NoF model stands at the opposite extreme as AGN, allowing for unimpeded transformation of gas into stars in regions able to collapse and condense into galaxies. Although unrealistic as a galaxy formation model, it serves to provide a useful framework where the relative importance of feedback effects may be gauged and understood.

Table 2 summarizes the relevant parameters of each feedback implementation. For ease of reference, we also quote in each case, the name used to label each simulation by Schaye et al. (2010).

3   NUMERICAL RESULTS

3.1   The halo sample

Our sample consists of all galaxies at the centers of haloes with virial mass[1] $M_\mathrm{vir} > 10^{11}\, h^{-1}\, M_\odot$. There are about 150 haloes at $z = 2$ in each $25\, h^{-1}$ Mpc-box OWLS run with masses between $10^{11}\, h^{-1}\, M_\odot < M_\mathrm{vir} < 3 \times 10^{12} h^{-1} M_\odot$. The median of the sample is $M_\mathrm{vir} \sim 1.8 \times 10^{11} h^{-1} M_\odot$. Halos are identified by the substructure finding algorithm SUBFIND (Springel et al. 2001; Dolag et al. 2009) and centers are defined by the minimum of the potential. All runs use the same initial conditions, and therefore the number (and identity) of haloes selected for analysis is roughly the same in each simulation.

We begin with an overview of the properties of the gaseous component within the virial radius and its halo mass dependence (Sec. 3.2), and follow on with a description of the properties of the stellar component of the central galaxy (Sec. 3.3). We discuss the link between feedback and morphology in Sec. 3.4, and compare the number of massive galaxies in various runs in Sec. 3.5. We end this section by discussing the mass and angular momentum of central galaxies, as well as their dependence on feedback (Secs. 3.6 and 3.7), before proceeding to compare these results with observations.

3.2   Gas within the virial radius

Fig. 1 illustrates the distribution of gas within the virial radius in four haloes selected from the WF2 run at $z = 2$. Each panel corresponds to haloes differing by consecutive factors of two in virial mass. The box size in each panel has been adjusted to the virial radius of each halo. Only gas particles within the virial radius are shown, and have been colored according to their density/temperature.

Red particles are those with temperatures exceeding $(1/4)\, T_\mathrm{vir}$, where $T_\mathrm{vir} = 35.9\, (V_\mathrm{vir}/\mathrm{km}\ \mathrm{s}^{-1})^2$ K is the virial temperature of a halo (V_vir is the circular velocity at r_vir). Gas particles in this "hot phase" are all found in a low-density, largely pressure-supported atmosphere that fills the halo out to the virial radius. The virial temperature is $\sim 10^6$ K for haloes with $V_\mathrm{vir} \sim 170$ km/s, about the median virial velocity range spanned by our sample.

The fraction of gas in the hot phase increases with halo mass; it makes up 68% of all the gas within r_vir in the most massive halo but only 21% in the least massive system shown in Fig. 1 . This is a result of the steady increase in cooling time with increasing halo mass, which favors the formation of a hot tenuous gas atmosphere in massive systems.

Particles in green are those in the "warm" phase, which we define as those satisfying $3 \times 10^4 \mathrm{K} < T < (1/4)\, T_\mathrm{vir}$. These are particles at moderate overdensities, and make up a small fraction of all the gas within r_vir; from $\sim 7\%$ in the most massive halo to $\sim 15\%$ in the least massive one. This gas typically traces material accreted relatively recently, which has yet to be pressurized by shocks, or material ejected during accretion events in "tidal tails" that expand and cool as they recede from the center. Because accretion occurs frequently through filaments, and tidal tails are like-

---

[1] Virial values are measured at or within the virial radius, r_vir, of a halo, defined as the radius where the mean inner density exceeds the critical density of the universe by a factor $\Delta_\mathrm{vir}(z) = 18\pi^2 + 82f(z) - 39f(z)^2$. Here $f(z) = [\Omega_\mathrm{M}(1+z)^3/(\Omega_\mathrm{M}(1+z)^3 + \Omega_\Lambda)] - 1$ and $\Omega_\mathrm{M} = \Omega_\mathrm{CDM} + \Omega_\mathrm{bar}$ (Bryan & Norman 1998). $\Delta_\mathrm{vir} \sim 170$ at $z = 2$ for our choice of cosmological parameters.
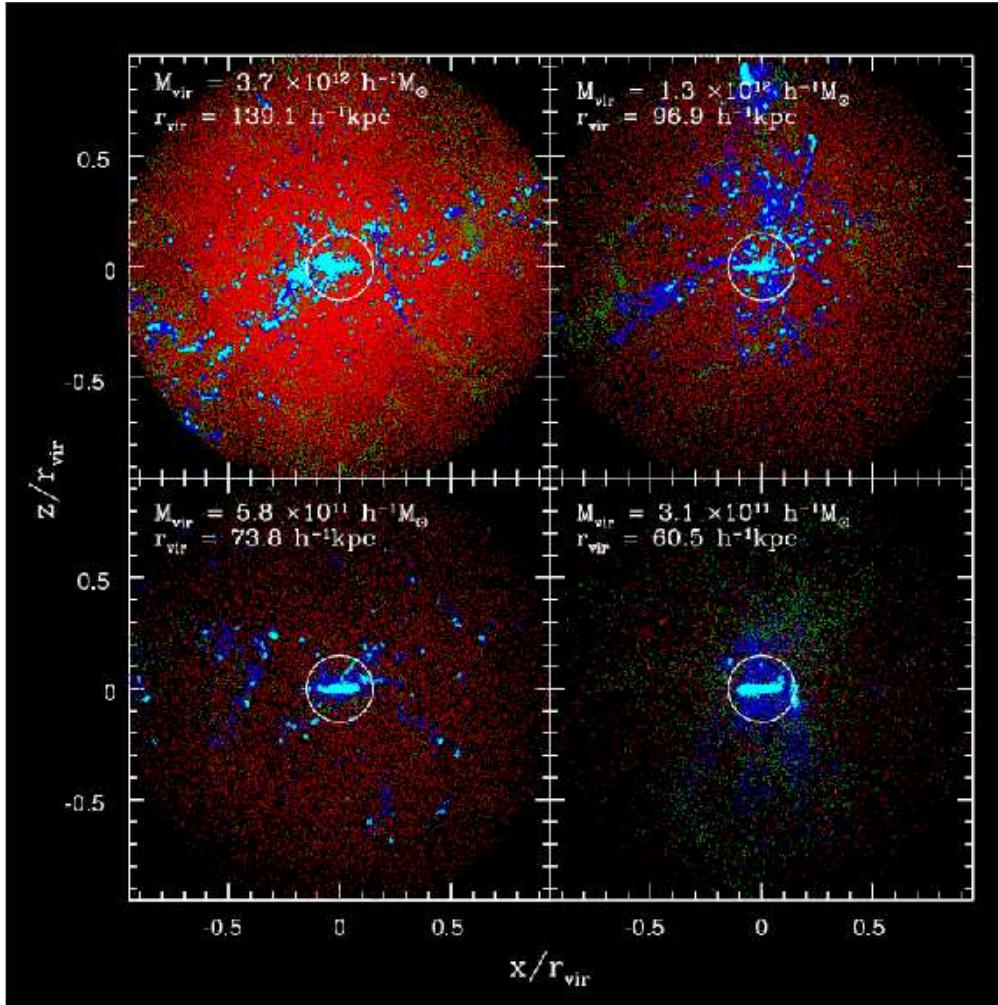
Figure 1. Gas particles within the virial radius of four WF2 haloes spanning the mass range of systems selected for analysis. The virial mass and radius are given in the label of each panel. Gas particles are colored according to temperature: red, green, and blue correspond to particles in the hot, warm, and cold phases, respectively. Hot particles are those with $T > (1/4)T_{\rm vir}$, where $T_{\rm vir} = 35.9(V_{\rm vir}/\,{\rm km\,s^{-1}})^2$ K is the virial temperature of the halo. Cold particles are those with $T < 3 \times 10^4$ K. Warm are those with intermediate temperatures. Cyan particles denote dense, star-forming gas in the PEOS phase. Particles are plotted sequentially in order of descending temperature, so colder particles may occult hotter ones in regions of high density. Small circles show the radius, $r_{\rm gal} = 0.15\,r_{\rm vir}$, used to define the central galaxy.

wise highly asymmetric, the warm component distribution is non-uniform, with discernible large-scale features suggestive of recent mergers and accretion events.

Cold ($T < 3 \times 10^4$ K) gas of moderate density ($n < n_c = 0.1$ cm^{-3}) is shown in blue, and is rather clumpy in appearance. Large-scale features similar to those noted for the warm component are also visible here, suggesting that this is also mostly gas recently accreted or affected by accretion events. In terms of mass, this component is negligible ($\sim 5\%$) in the $3.7 \times 10^{12}\,h^{-1}\,M_\odot$ halo but increases in importance with decreasing halo mass. Indeed, it makes up $\sim 30\%$ of all the gas in the $3.1 \times 10^{11}\,M_\odot$ halo shown in Fig. 1.

The star-forming gaseous component is, by definition, the densest ($n > n_c = 0.1$ cm^{-3}), and is shown in cyan in Fig. 1. Most of this gas is at the bottom of the potential well of the main halo and of its substructure haloes, and makes up between 20 and 30% of the gas within $r_{\rm vir}$, with little dependence on halo mass.

The generally strong halo mass dependence of the various gaseous phases highlights the different modes of accretion that shape the evolution of a central galaxy. In massive haloes galaxies

grow by accreting cooled material from the surrounding reservoir of hot gas, whereas in low mass haloes the gas is likely to flow virtually unimpeded to the central regions, where it may be swiftly accreted into the central galaxy (White & Frenk 1991; Kereš et al. 2005; Dekel & Birnboim 2006; Birnboim et al. 2007; Kereš et al. 2009; Brooks et al. 2009). These different accretion modes highlight the complex assembly history of a galaxy, a complexity that is further compounded by the effects of feedback that we discuss below.

3.3 Central galaxies

Fig. 2 shows a zoomed-in view of the four WF2 haloes depicted in Fig. 1, including the stellar component, which is shown in yellow. The circle centered on the main galaxy indicates the radius, $r_{\rm gal} = 0.15\,r_{\rm vir}$, that we use to define the central galaxy inhabiting each halo. As is clear from the figure, this definition includes virtually all stars and dense gas obviously associated with the galaxy.
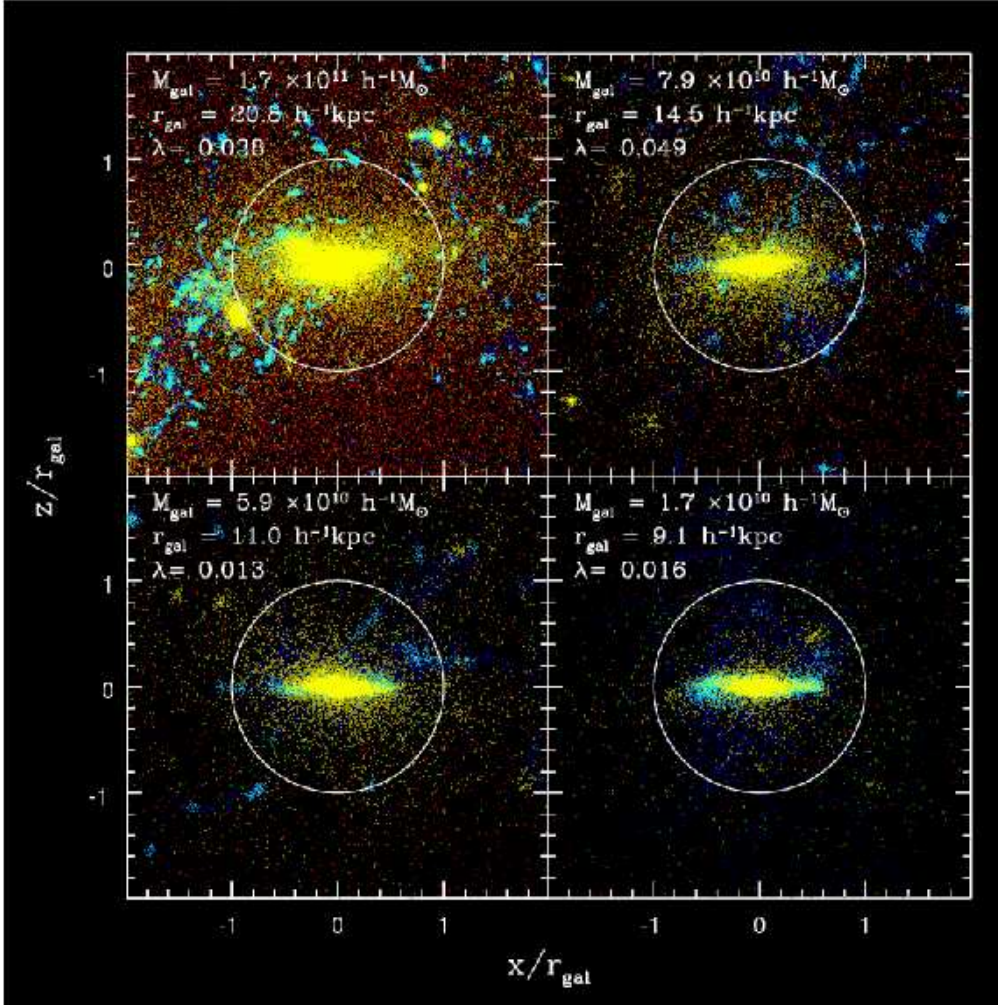
Figure 2. Zoomed-in view of the galaxies at the centers of the haloes shown in Fig. 1. Colors are as described in the caption of that figure, except that yellow now denotes "star" particles. The circles show the galaxy "radius", $r_{\rm gal} = 0.15\,r_{\rm vir}$. Each box has been rotated so that the spin axis of the PEOS gas is aligned with the z axis of each panel. This "edge-on" projection emphasizes the presence of disk-like structures in all four haloes. Besides $r_{\rm gal}$, labels in each panel specify the baryonic mass of the galaxy, $M_{\rm gal}$, and the spin parameter of the surrounding halo, λ.

It also emphasizes the halo mass dependence of the various phases in which baryons may flow into the central galaxy. As discussed above, whereas galaxies in low mass haloes grow through the smooth accretion of cold gas, a fair fraction of the star forming gas in the most massive systems include "clouds" that condense out of the hot and warm phases. Little star formation happens in these clouds, however, since their typical densities are well below those reached in the main body of the galaxy.

Gas turns swiftly into stars once it settles into a dense, thin, rotationally supported disk in the central galaxy. In systems that avoid major mergers, the stellar component inherits the disk-like structure of the gaseous component. All 4 galaxies shown in Fig. 2 sport well-defined stellar disks, which have been rotated to be seen "edge-on" in this figure. Disks of gas and stars are indeed quite common in the WF2 run that we have chosen to illustrate the main general features of our simulated galaxies.

3.4 Feedback and morphology

Varying the feedback implementation has a dramatic effect on the properties of central galaxies. We illustrate this in Figs. 3 and 4,

where we show, for the *same* dark matter halo, how the appearance of its central galaxy varies with feedback. Although the assembly history of the dark halo is identical in all cases, differences in feedback lead to drastic variations in the stellar mass, gaseous content, and morphology of the central galaxy.

When feedback is inefficient, such as in the ThF and WF4 runs, a stellar disk is clearly present, but its mass is small compared with that of the spheroidal component. This is because most stars form in early collapsing protogalaxies which are later stirred into a spheroidal component when these subsystems coalesce to form the final galaxy. The extreme case is NoF, where the absence of feedback allows for early and highly efficient star formation that converts most of the available gas into stars. The large number of satellites seen around the NoF central galaxy is also a result of the lack of feedback. This preserves star formation even in small subhaloes, where modestly energetic feedback might lead to drastic changes in the availability of star formation fuel and in the total mass of stars formed.

When feedback effects are strong, such as in the WF2Dec, WDENS, and AGN runs, fewer stars form since the gas is constantly pushed out of star-forming galaxies by outflows. These out-
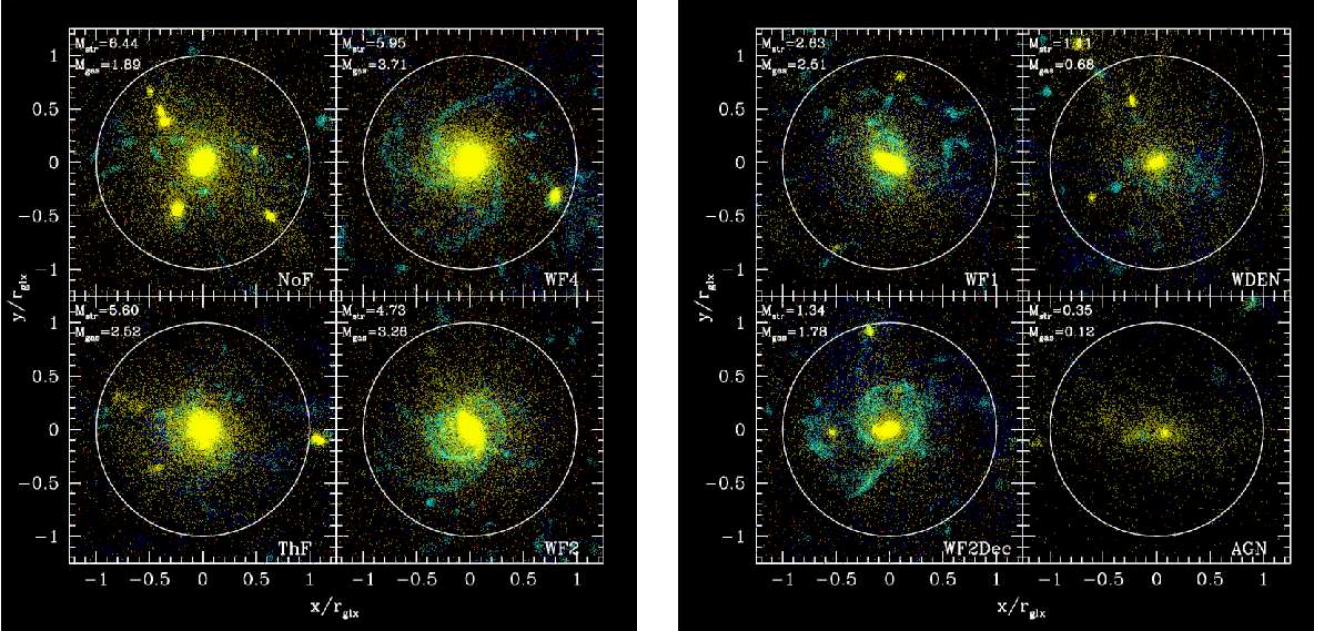
Figure 3. Face-on view of the central galaxy formed at the center of an $M_{\rm vir} = 1.2 \times 10^{12} \, h^{-1} \, M_\odot$ halo. All panels correspond to the *same* halo, but in runs with different feedback implementations, as labelled in the bottom right of each panel. Only baryonic particles are shown. Colors indicate gas temperature, classified as hot (red), warm (green), cold (blue) and star-forming (cyan). See the caption to Fig. 1 for details. Yellow dots correspond to "star" particles. The circle in each panel indicate the radius used to define the central galaxy, $r_{\rm gal}$. Each galaxy has been rotated so that it is seen "face on"; i.e., the angular momentum of the PEOS gas is aligned with the line of sight of the projection. The mass in stars and gas within $r_{\rm gal}$ is labelled in each panel (units are $10^{10} \, h^{-1} \, M_\odot$).

Figure 4. Same as Fig. 3, but each galaxy has been rotated so that it is seen "edge-on". Labels in each panel give the fraction of kinetic energy of the stellar component in ordered rotation.

flows also disrupt the smooth settling of gas into disks and its gradual transformation into stars. In the most extreme case (AGN), the gas outflows are so violent that there is little gas left in the central galaxy. In none of these cases do central galaxies have an extended and easily recognizable stellar disk component.

As may be seen from Fig. 4, more moderate feedback im-

plementations, such as WF2 and WF1, yield systems with a well-defined stellar disk, and a gas/stellar mass fraction of roughly 1:1.

This impression is corroborated quantitatively by the fraction of *stellar* kinetic energy in ordered rotation:

$$\kappa_{\rm rot}^{\rm str} = K_{\rm rot}/K; \quad \text{with} \quad K_{\rm rot} = \sum (1/2) {\rm m} ({\rm j_z/R})^2 \qquad (1)$$
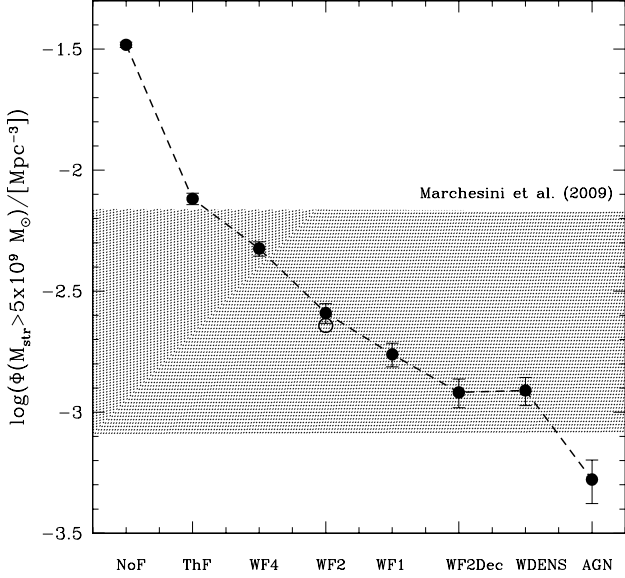
Figure 5. Number density of galaxies with stellar mass exceeding $5 \times 10^9 \, M_\odot$, shown for the various feedback implementations explored in this paper. Runs are labeled as in Table 2, and are listed in the abscissa roughly in order of increasing feedback efficiency. The open circle correspond to the WF2 low resolution run WF2LR. "Error bars" denote $\sqrt{N}$ uncertainties corresponding to the number of systems in our computational box. The shaded area outline observational constraints from estimates of the galaxy stellar mass function at $z = 2$, as compiled by Marchesini et al. (2009). Note the strong decline in the number of massive galaxies as a function of increasing feedback efficiency.

Here, m is the mass of a star particle; j_z is the z-component of the specific angular momentum, assuming that the z-axis coincides with the angular momentum vector of the galaxy, and R is the (cylindrical) distance to the z-axis. $\kappa_{\rm rot}$ is listed in each panel of Fig. 4 for the stellar component: it is highest for WF2, and minimum for AGN.

3.5 Feedback and massive galaxies

A robust way of assessing the effectiveness of the various feedback implementations explored in these runs is to compute the abundance of massive galaxies that each predicts. Because the total amount of stars formed decreases as the feedback becomes more effective, the abundance of massive galaxies is expected to depend sensitively on feedback. This is shown in Fig. 5, where we plot, for each implementation, the number of galaxies (per unit volume) with stellar masses exceeding $5 \times 10^9 \, M_\odot$. This mass threshold is chosen to roughly coincide with $10,000$ baryonic particles

The runs in Fig. 5 are ranked, from left to right, in order of decreasing number of massive galaxies (i.e., increasing feedback efficiency). This figure confirms the strong effect of feedback on the abundance of massive galaxies. For example, the AGN run has ~ 16 times fewer such galaxies than the run with only thermal feedback, ThF, and ~ 60 fewer than NoF, the model without feedback energy injection.

Not only does the total amount of feedback energy matter, but also the manner in which it is injected. Indeed, large differences are also obtained for models with the *same* feedback strength (as mea-

sured by the total feedback energy per unit stellar mass formed), but that differ in the combinations of mass loading and wind velocities: ThF, WF4, WF2, WF1, WF2Dec and WDENS all assume that 40% of the available supernova energy is invested into winds, yet their predictions for the number of bright galaxies differ by up to a factor of ~ 4.

The results do not seem to depend dramatically on numerical resolution, as shown by the good agreement between the WF2 and WF2LR runs (the latter is shown with an open symbol in Fig. 5). Reducing the number of particles by a factor of eight (as in WF2LR) brings down the number of $M_{\rm gal} > 5 \times 10^9 \, M_\odot$ galaxies in the box from 133 to 123. The trends shown in Fig. 5 are therefore unlikely to be an artifact of limited numerical resolution.

The shaded band in Fig. 5 indicates the expected number of massive galaxies, taken from Marchesini et al. (2009), after interpolating their fits to $z = 2$ and correcting volume elements to account for the different cosmology assumed in their work. The band aims to represent uncertainties due to photometric redshift inaccuracies and cosmic variance. This is almost certainly optimistic, since additional uncertainties, such as those stemming from the choice of IMF, have not been included. Furthermore, the bright end of the luminosity function traces the abundance of the most massive objects present at $z = 2$ and is, as such, particularly sensitive to the adopted cosmological parameters.

Given these large uncertainties, it would be premature to use Fig. 5 to rule in or out any particular implementation of feedback but, as the data improve, it might be useful to revisit this issue to learn which feedback modeling procedure is favored or disfavored by the data. For clarity, many of the plots in the analysis that follows will focus on 4 cases that span the full range of feedback strength shown in Fig. 5: i.e., NoF, WF2, WF2Dec, and AGN.

We end by noting that different observational diagnostics, such as the specific star formation rate or the gas content as a function of galaxy luminosity, could be used to provide further constraints on the viability of each feedback model. We plan to present a detailed analysis along these lines in a future paper (see Haas et al., *in preparation*).

3.6 Galaxy masses

The stellar and gaseous masses of galaxies assembled at the centers of dark matter haloes are determined largely by the virial masses of the systems, modulated by the efficiency of radiative cooling and the regulating effects of feedback. We show this in the left panel of Fig. 6 for all galaxies selected from the WF2 run. The dots in the figure correspond to $M_{\rm gal}$, the total baryon mass within the radius, $r_{\rm gal}$, used to define the central galaxy; the solid line traces the median as a function of $M_{\rm vir}$. As expected, the central galaxy mass correlates well with $M_{\rm vir}$, albeit with fairly large scatter (the global rms about the median trend is ~ 0.19 dex).

The top dashed line in this panel indicates the mass, $f_{\rm bar} M_{\rm vir}$, galaxies would have if all baryons in the halo have assembled at the center (the universal baryon fraction is $f_{\rm bar} = \Omega_b/\Omega_M = 0.175$). The thick dotted magenta line shows the median baryon mass within $r_{\rm vir}$ as a function of halo mass. This shows that massive systems have retained all baryons within the virial radius, but also that the effects of feedback are clear at the low mass end: $10^{11} \, h^{-1} \, M_\odot$ haloes have only retained about half of their baryons within the virial radius. Of those, only one third or so have collected in the central galaxy.
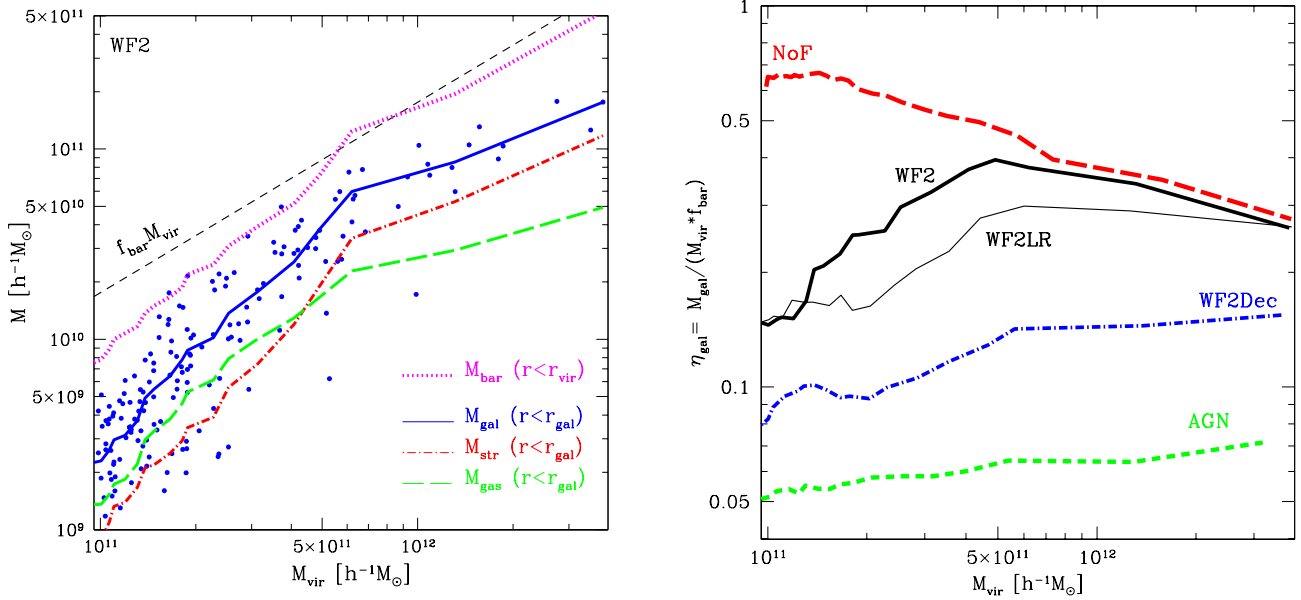
Figure 6. *Left:* Central galaxy mass as a function of virial mass for all haloes selected in the WF2 run. The top dashed line indicates the mass in baryons in each halo corresponding to the universal baryon fraction, $f_{\rm bar} = \Omega_b/\Omega_M = 0.175$, adopted in the simulations. Dots correspond to the baryon mass of the central galaxy (i.e.; within $r_{\rm gal}$); the thick solid (blue) curve tracks its median as a function of $M_{\rm vir}$. The two bottom curves track the median for the stellar (red, dot-dashed) and gaseous (green, dashed) mass within $r_{\rm gal}$. The thick dotted (magenta) line shows the median of the total mass in baryons within the virial radius, $r_{\rm vir}$. *Right:* Galaxy formation "efficiency", $\eta_{\rm gal} = M_{\rm gal}/(f_{\rm bar} M_{\rm vir})$, as a function of halo virial mass for the various runs. For clarity, only the results corresponding to 4 selected runs are shown, spanning the effective range of feedback strength, from the "no feedback" (NoF) case to the AGN case, where feedback effects are maximal. Cases not shown fall between these two extremes. The scatter around each curve is large, typically ~ 0.19 dex rms. The thin line labelled WF2LR has the same physics are WF2 but $8\times$ poorer mass resolution and $2\times$ lower spatial resolution. Note that the galaxy formation efficiency is, on average, very sensitive to feedback, but only weakly dependent on halo mass, at least for the range of masses considered here.

Thus, the "efficiency" of galaxy formation, as measured by the mass of the galaxy expressed in units of the total baryon mass corresponding to its halo, $\eta_{\rm gal} = M_{\rm gal}/(f_{\rm bar} M_{\rm vir})$, increases steadily with halo mass, from $\sim 10\%$ in $10^{11}\,h^{-1}M_{\odot}$ haloes to a maximum of roughly 40% for $M_{\rm vir} \sim 5 \times 10^{11}\,h^{-1}M_{\odot}$. There is also indication that the efficiency decreases in more massive systems, to roughly $\sim 30\%$ in the most massive haloes.

These trends (i.e., low galaxy formation efficiency in low and high mass haloes) are qualitatively in line with what is required to reconcile the shape of the galaxy luminosity function with the dark matter halo mass function (see, e.g., Yang et al. 2005; Conroy & Wechsler 2009; Guo et al. 2010). Feedback is the main mechanism responsible for reducing efficiency in low-mass haloes. Together with long cooling timescales, it also helps prevent the formation of too massive galaxies in high-mass haloes.

Although the trends seem qualitatively correct, it remains to be seen whether a model like WF2, evolved to $z = 0$, is able to satisfy the stringent constraints placed by the stellar mass function in the local Universe. Indeed, the recent estimate of Li & White (2009) suggest that only 3.5% of all baryons in the Universe are today locked up in stars, and McCarthy et al. (2009) argue that supernova feedback alone is not enough to ensure such a low efficiency of transformation of baryons into stars. Since the runs we analyze here have only been evolved to $z = 2$, we are unable to address this issue in a conclusive manner, but we plan to return to it when extending the present analysis to the GIMIC simulations.

3.6.1 Feedback dependence

The right panel of Fig. 6 shows that the overall efficiency of galaxy formation is quite sensitive to feedback. Each curve here tracks the median trend of $\eta_{\rm gal}$ with $M_{\rm vir}$ for different runs. As expected from the discussion of Fig. 5, $\eta_{\rm gal}$ is highest for NoF and lowest for AGN, with more moderate results for WF2 and WF2Dec, as well as the other runs, which are omitted from this panel for clarity.

Clearly, not only the total feedback energy input, but also the details of its implementation can affect dramatically the galaxy formation efficiency. Central galaxies in the NoF case can be up to $10\times$ more massive than in the AGN run. WF2 galaxies are a factor of two to three more massive than those formed in WF2Dec, although the only difference between these two runs is the choice to "decouple" hydrodynamically the supernova-driven winds in the latter. The reasonable agreement (given the large scatter) between WF2 and WF2LR suggests that this result is not unduly influenced by numerical resolution.

Although the average galaxy formation efficiency depends strongly on feedback, its dependence on halo mass is weak: $\eta_{\rm gal}$ varies by less than a factor of 2 over the factor of ~ 30 range in virial mass spanned by the simulations. In the absence of feedback $\eta_{\rm gal}$ peaks at low masses: feedback is clearly needed to counter the high efficiency of gas cooling in low mass haloes. We highlight however that the dependence of $\eta_{\rm gal}$ on halo mass must become significantly stronger for halo masses below those studied here (i.e. $M_{\rm vir} < 10^{11}h^{-1}M_{\odot}$) in order to successfully reproduce the measured faint end of the luminosity function.
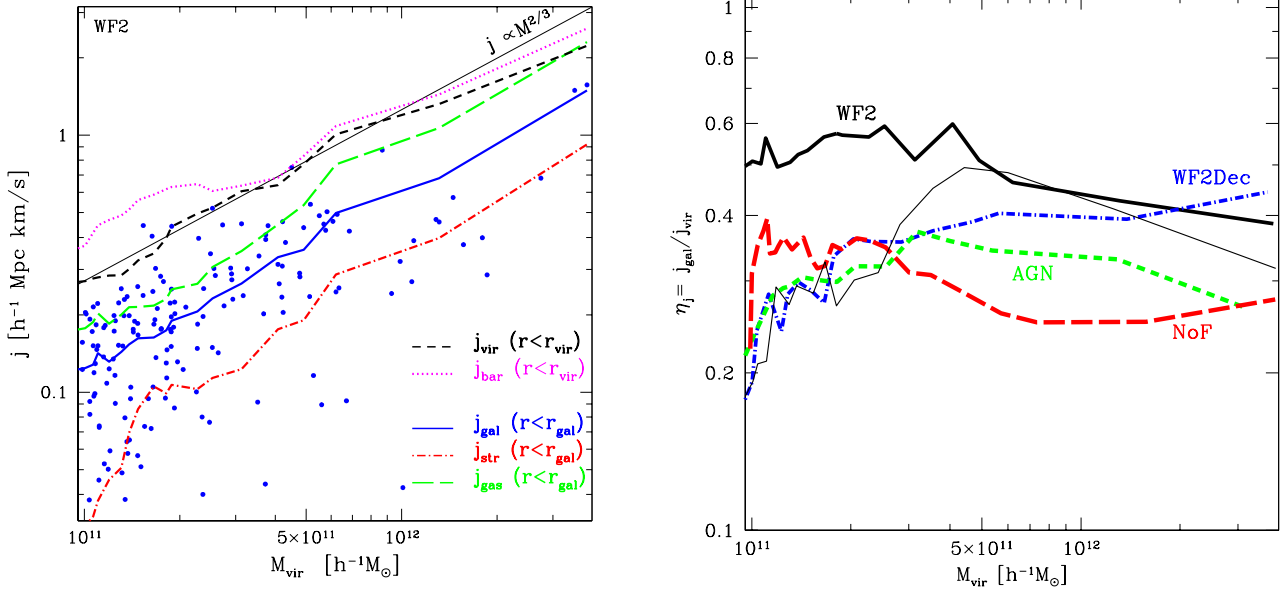
Figure 7. *Left:* Specific angular momentum, j, as a function of virial mass. The black dashed line tracks the median j of the dark matter component as a function of $M_{\rm vir}$. This follows closely the $j \propto M^{2/3}$ correlation expected for systems with constant spin parameter, λ. The other symbols, colors, and line types are the same as in Fig. 6. Note that the specific angular momentum of *all* baryons within $r_{\rm vir}$ is quite similar to that of the halo as a whole (top dotted curve). The specific angular momentum of the central galaxy is typically lower than that of the halo; although it correlates well with $M_{\rm vir}$, the scatter is large. *Right:* Angular momentum "efficiency", $\eta_j = j_{\rm gal}/j_{\rm vir}$, as a function of mass for various runs. For clarity, only the median of galaxies in runs NoF, WF2, WF2Dec, and AGN, are shown as a function of mass. Note that, unlike $\eta_{\rm gal}$, the angular momentum efficiency, η_j, is a weak function of both mass and of feedback. See text for further discussion.

3.7 Galaxy Angular Momentum

The size and rotation speed of galaxy disks place powerful observational constraints on galaxy formation models, and are directly linked to the angular momentum acquired and retained by the baryons that make up the galaxy. We explore this in Fig 7, where we show, in the left panel, the specific angular momentum of the various galaxy components as a function of halo virial mass.

As in Fig. 6, dots correspond to the baryonic component inside $r_{\rm gal}$ for individual systems in run WF2. Although the scatter is large (an rms of ~ 0.27 dex), the solid curve, which tracks the median j as a function of $M_{\rm vir}$, shows that the specific angular momentum scales roughly like $j \propto M^{2/3}$. This is the same scaling found for the dark matter component within $r_{\rm vir}$ (dashed black line), and is indeed the expected scaling if the dimensionless halo spin parameter, $\lambda = J|E|^{1/2}/GM^{5/2}$, is constant.

When all baryons within the virial radius are considered, their specific angular momentum agrees well with that of the dark matter (magenta dotted line). On the other hand, the specific angular momentum of central galaxies is, on average, about 50% that of its surrounding halo. This fraction, which we refer to as the "angular momentum efficiency", $\eta_j = j_{\rm gal}/j_{\rm vir}$, appears, on average, to be roughly independent of halo mass for WF2 galaxies.

Interestingly, the gaseous and stellar components of WF2 galaxies have distinctly different angular momenta. The gas has 2 to 3 times larger specific angular momentum than the stars, implying that the radial extent of gaseous disks in these galaxies is substantially larger than that of the stellar component. This was already noted by Sales et al. (2009) as a possible way to explain the large sizes of the $z = 2$ star-forming (gaseous) disks analyzed by the SINS survey (Förster Schreiber et al. 2009). We shall return to this issue in Sec. 4.

3.7.1 Feedback dependence

The feedback dependence of the angular momentum efficiency, η_j, is shown in the right panel of Fig. 7 as a function of virial mass. Like the galaxy formation efficiency, $\eta_{\rm gal}$, the halo mass dependence of η_j is weak. Unlike $\eta_{\rm gal}$, however, η_j depends only weakly on feedback. In a given halo, NoF galaxies have approximately the *same* angular momentum as galaxies in the AGN run. This is striking, since their baryonic masses differ on average by a factor of ~ 10. Feedback affects the mass of a galaxy much more severely than its spin: 9 out of 10 baryons in NoF galaxies are missing from AGN galaxies, but their specific angular momenta are, on average, the same.

The thin line in the right panel of Fig. 7 shows the results for WF2LR. Despite the large scatter, numerical resolution effects are clearly noticeable below $\sim 4 \times 10^{11} h^{-1} M_\odot$. This corresponds to $\sim 10^4$ particles per halo for WF2LR; extrapolating this to WF2, it would mean that our results there should be credible down to $\sim 5 \times 10^{10} h^{-1} M_\odot$. It would therefore appear as if the main trends shown in Fig. 7 are safe from resolution-induced numerical artifacts.

The angular momentum efficiency peaks in moderate feedback runs (such as WF2) at roughly 50% and its dependence on feedback strength is non-monotonic. Despite this apparent complexity, galaxy masses and angular momenta are actually well correlated. Following Sales et al. (2009), we define the mass and angular momentum *fractions* m_d and j_d, as

$$m_d = \eta_{\rm gal} f_{\rm bar} = M_{\rm gal}/M_{\rm vir}, \qquad (2)$$

and

$$j_d = \frac{J_{\rm gal}}{J_{\rm vir}} = \frac{M_{\rm gal} j_{\rm gal}}{M_{\rm vir} j_{\rm vir}} = \eta_{\rm gal} \eta_j f_{\rm bar} \qquad (3)$$

These parameters were introduced by Mo et al. (1998), and have become standard fare in semianalytic models of disk galaxy formation.

Sales et al. (2009) noted that j_d and m_d correlate well, but in a manner different from the typical $j_d = m_d$ assumption of semianalytic models (e.g., Cole et al. 2000) and, perhaps more importantly, insensitive to feedback. These authors showed that the simple expression

$$j_d = 9.71 \, m_d^2 \left(1 - \exp[-1/(9.71 \, m_d)]\right) \qquad (4)$$

provides a good approximation to the results of four OWLS runs with supernova-driven winds: WF1, WF2, WF4 and WF2Dec.

We revisit this result in Fig. 8, where we show the j_d-m_d correlation for all the OWLS runs considered in this paper. The dots show individual WF2 galaxies, and are meant to illustrate the typical scatter in the relation; the curves trace the median trend of j_d with m_d for the different runs while the black dotted curve outline the relation in Eq. 4. Although the AGN and NoF galaxies deviate somewhat from the trend outlined in eq. 4 (indicated by the dotted thick line), the departures are relatively small and the agreement between runs seems remarkable given the extreme range in feedback models explored here.

The bottom panel in Fig. 8 shows the *distribution* of m_d for four different feedback implementations. Clearly, feedback, at least as implemented in our models, affects mostly the baryonic mass of galaxies, but largely preserves the link between the spins of haloes and galaxies. This link imprints correlations between galaxy mass, size, and rotation speed that may be contrasted with observations. We turn to this issue next.

Figure 8. *Top:* The angular momentum fraction $j_d = J_{\mathrm{gal}}/J_{\mathrm{vir}}$ vs the galaxy mass fraction, $m_d = M_{\mathrm{gal}}/M_{\mathrm{vir}}$. Dots correspond to individual galaxies in WF2 and are meant to illustrate the scatter; the median trend is traced by the black solid line. Other curves are analogous, but for each feedback model analyzed here. The black dotted curve is the fit proposed by Sales et al. (2009). The straight line labeled $j_d = m_d$ corresponds to the commonly-adopted assumption that the specific angular momentum of a galaxy equals that of its surrounding halo. *Bottom:* Distribution of galaxy mass fraction, m_d, for four different runs spanning the range of feedback strengths of our simulations: NoF, WF2, WF2Dec, and AGN.

4 OBSERVATIONAL DIAGNOSTICS

4.1 Size and Stellar Mass of $z = 2$ Galaxies

The feedback-driven trends of galaxy mass and angular momentum efficiencies discussed above imprint different relations between the stellar mass, M_{str}, and the size of a galaxy. This is shown in Fig. 9, where the various panels compare (for runs NoF, WF2, WF2Dec, and AGN) the half-mass radius of the galaxy versus M_{str}. The panels on the left show the the half-mass radius of the gas component whereas those on the right correspond to the stars. The thick solid curve in each panel traces the median trend as a function of M_{str}. As noted above, simulated galaxies are substantially more extended in gas than in stars.

The simulated galaxies are contrasted with data for the large star-forming gas disks studied by the SINS survey (Förster Schreiber et al. 2009, hereafter FS09), as well as with the quiescent compact red galaxies of van Dokkum et al. (2008, hereafter vD08). These two datasets probably bracket the extremes in the size distribution of massive galaxies at $z = 2$, from the most extended to the most compact.

When feedback is inefficient (e.g., the NoF run) most stars form in dense, early-collapsing progenitors that merge later on to form the final galaxies. During such mergers the baryonic component transfers angular momentum to the surrounding halo, leading to the formation of very compact massive galaxies (Navarro & Benz 1991; Navarro et al. 1995; Navarro & Steinmetz 1997). The galaxies that result are therefore nearly as compact as the quiescent vD08 spheroids, although we note that many of those
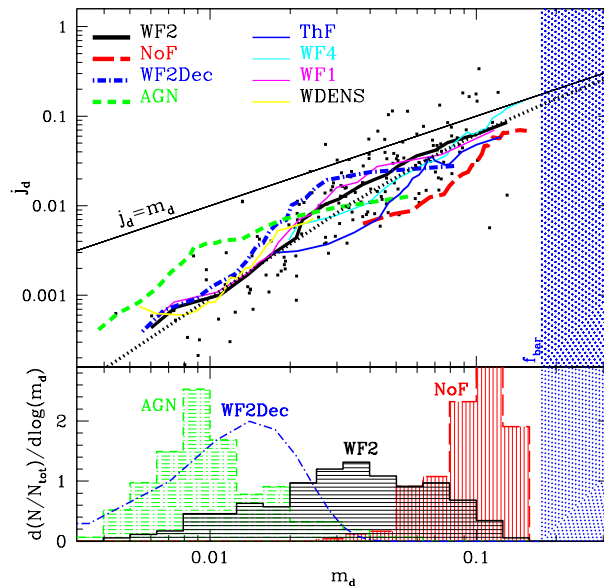
simulated galaxies have half-mass radii even smaller than the gravitational softening of our simulations, so their true sizes are actually uncertain. The gaseous component in these simulations is also quite compact, with radii rarely matching those of SINS disks.

Intermediate strength feedback (e.g., the WF2 run) has little effect on the most massive galaxies, which are generally as compact as the vD08 spheroids. On the other hand, feedback affects more strongly less massive systems, leading to a correlation between the mass and size of the stellar component where, at the massive end, size decreases with increasing mass. This trend runs counter the well-established galaxy scaling laws at z=0 (brighter galaxies tend to be bigger). The trend is reversed at lower masses and results, overall, in systems whose gaseous disks overlap in properties with those of galaxies in the SINS survey.

Increasing the effects of feedback (as in the WF2Dec and AGN runs) continues this trend, gradually reducing the mass of galaxies and increasing their size at given M_{str}. This is because the more efficient the feedback the more massive the halo inhabited by a galaxy of given stellar mass. More massive haloes are larger and have higher specific angular momenta. Since, as we saw above, galaxies generally inherit the specific angular momenta of their surrounding haloes, it is possible to have fairly large galaxies of modest stellar mass because they actually inhabit large, massive haloes. Indeed, many gaseous disks in the AGN run are even more extended than the rather extreme examples surveyed by SINS.
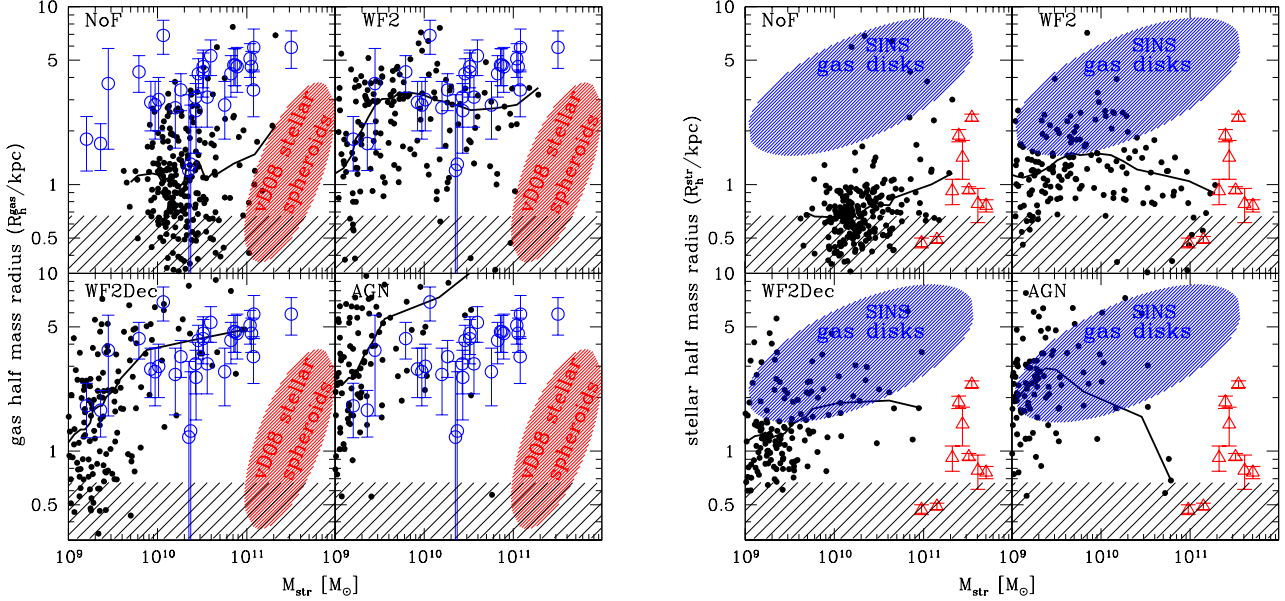
Figure 9. *Left:* half-mass radius of the gas as a function of stellar mass. Solid black dots in each panel show the results for four of our simulations NoF, WF2, WF2Dec and AGN. The thick solid line tracks the median as a function of mass. Open symbols with error bars correspond to the extended star-forming disk galaxies from the SINS survey (Förster Schreiber et al. 2009), while the red shaded ellipsoid indicates the area of the plot occupied by the sizes of the compact quiescent galaxies from van Dokkum et al. (2008). *Right:* same as before, but for the half-mass radii of the stars. In this case, open symbols and error bars are used to indicate the sizes of the compact stellar spheroids from van Dokkum et al. (2008), while the shaded blue area indicates the region of the plot occupied by extended gaseous disks from the SINS sample. The extended disks reported by SINS (Förster Schreiber et al. 2009) and the compact spheroidal galaxies from van Dokkum et al. (2008) probably bracket the size distribution of massive galaxies at $z = 2$. The black shaded area indicates the gravitational softening of the simulations. Half-mass radii for the gaseous components of simulated galaxies are typically larger than for the stars. Note that the size-stellar mass correlation is heavily dependent on feedback. When feedback is very efficient (e.g., WF2Dec/AGN) the size of the gaseous disks increase with stellar mass, a correlation that is reversed when feedback efficiency is low.

4.2 The Tully-Fisher Relation at $z = 2$

The structural diversity of $z = 2$ galaxies discussed above should also be manifest in their kinematics. We explore this in Fig. 10, where we plot, as a function of stellar mass, the circular velocity estimated for SINS galaxies and for the compact vD08 galaxies. For SINS, we use the "maximum" gas rotation speed, as quoted by FS09, whereas for vD08 we estimate the circular velocity at the effective radius based only on the contribution of the stellar component; i.e., $V_c^2 = G(M_{str}/2)/R_{eff}$. This is clearly a *lower limit* to the circular velocity at that radius, since it neglects the possible contributions of dark matter and gas components. We note this in Fig. 10 by small arrows on the vD08 data points (open triangles).

It is clear from this rendition of the data that the two populations of $z = 2$ galaxies follow very different Tully-Fisher relations. At given stellar mass, the compact galaxies are expected to have circular velocities at least *twice* higher than SINS disks. Although kinematic data for such galaxies is scarce, van Dokkum et al. (2009) report a preliminary measurement of the velocity dispersion of one of these galaxies. The high velocity dispersion reported, ~ 510 km/s, agrees with this interpretation.

The circular velocity of the simulated galaxies is measured at the half-mass radius of the stellar (red solid curve) or the gaseous (blue dashed curve) component, respectively. The comparison between simulations and observations yields similar conclusions as in the previous subsection.

Inefficient or absent feedback (e.g., NoF) yields galaxies that are more concentrated than the SINS disks, and therefore have, at given stellar mass, typically higher circular velocities. Forming

large, extended disks is difficult in the absence of efficient feedback. By contrast, accounting for the compact spheroids studied by vD08 is relatively easy.

In the case of AGN or WF2Dec, the most efficient feedback schemes explored in Fig. 10, many simulated galaxies are as spatially extended as the SINS disks, and the good agreement extends to the Tully-Fisher relation for those galaxies. Few very massive galaxies form as a result of the efficient feedback, and very few of those that form are as compact as those in the vD08 sample.

More moderate feedback choices give intermediate results. We consider it encouraging that some galaxies in the WF2 runs overlap with both SINS and vD08 in Figs. 9 and 10. If these models are correct, then there should be a sizable population of galaxies at $z = 2$ with properties intermediate to the SINS disks and vD08.

To summarize, the results shown in Figs. 9 and 10 indicate that neither the extreme compact sizes of massive spheroids nor the large spatial extent of star-forming disks at $z = 2$ pose insurmountable challenges to the standard paradigm. Indeed, it is possible, with adjustments to the feedback algorithm, to reproduce either population without resorting to unusual halo spin or halo formation histories.

At the same time, reproducing the striking diversity in the observed sizes and masses of $z = 2$ galaxies with a single feedback recipe might be challenging, but we are encouraged by the large scatter in the properties of simulated galaxies at given stellar mass that arises naturally in *any* feedback model. The relative abundance of either population is still poorly constrained observationally, and our small simulation box might not be adequate to study or search
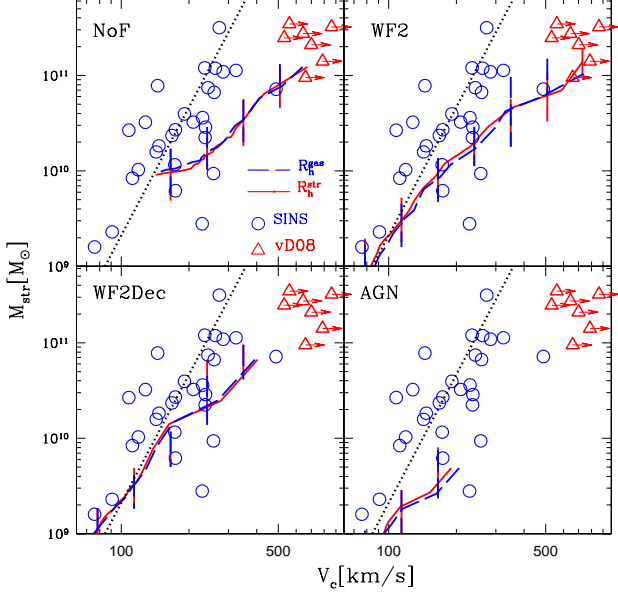
Figure 10. The stellar mass-circular velocity (Tully-Fisher) relation for $z = 2$ galaxies identified in runs with four different feedback implementations. Symbols are as in Fig. 9. The median circular velocity measured at the stellar half-mass radius is shown by the solid red line. Vertical lines show the 25-75 percentiles of the distribution. We also show this relation when the circular velocity is measured at the half-mass radius of the star forming gas (dashed blue curve). Open circles and triangles show the observational determinations for disks and compact galaxies at z=2 taken from Förster Schreiber et al. (2009) and van Dokkum et al. (2008). For the latter we assign velocities by neglecting the dark matter distribution; i.e., we assume $V_c^2 = G(M_{str}/2)/R_{eff}$, which constitutes a lower limit to the true circular velocity. This is indicated by the horizontal arrows in each panel. The thick dotted line is the Bell & de Jong (2001) relation for late-type galaxies at z=0 corrected to a Chabrier IMF.

for rare, extreme populations. Improved observational constraints on the relative abundance of extended vs compact galaxies and a better characterization of the "average" population of $z = 2$ galaxies will certainly help to constrain which feedback implementation gives results that agree best with observation.

4.3 Disks and Mergers at $z = 2$

Another interesting constraint is provided by the frequency of systems actively forming stars in rotationally-supported disks. Before surveys such as SINS and OSIRIS (Förster Schreiber et al. 2009; Law et al. 2009, and references therein) started to resolve the kinematics of star-forming galaxies at high z, it had been commonplace to assume that systems where star formation was progressing in earnest would almost invariably be ongoing major mergers. It is now clear, however, that at least about one third of the galaxies surveyed by SINS and OSIRIS are forming stars in relatively quiescent disks rather than ongoing mergers with disturbed and transient kinematics (for an alternative view, however, see Robertson & Bullock 2008).

We use κ_{rot}, the simple measure of the importance of ordered rotation introduced in Sec. 3.4, to explore this issue in our simulations. When most of the gas is in a rotationally-supported disk,

the parameter κ_{rot} should approach unity. Fig. 11 enables a visual calibration of this parameter by showing edge-on projections of 12 galaxies arranged by the value of κ_{rot} of the central galaxy (in this case only the star-forming gas is used to compute κ_{rot}). Figure 11 shows an image of the projected gas density within a sphere of radius $1.3\,r_{gal}$. Thin, extended disks are the norm when $\kappa_{rot} \gtrsim 0.75$. Ongoing mergers typically have $\kappa_{rot} \lesssim 0.5$; those with intermediate values of κ_{rot} have disturbed morphologies, and tend to be late-stage mergers or systems where accretion is ongoing but minor.

Using this simple measure, the fraction of ongoing mergers vs quiescent disks may be readily estimated, and is shown in the top panel of Fig. 12 for the case of WF2. The distribution of κ_{rot} for all WF2 galaxies is shown by the top histogram; the shaded histogram is for the same run, but reducing the sample of galaxies to one half by selecting only those in haloes more massive than $2 \times 10^{11} h^{-1} M_\odot$. Encouragingly, the shape of the two histograms is quite similar. This is further confirmed by the distribution of κ_{rot} in WF2LR galaxies (for $M_{vir} > 2 \times 10^{11} h^{-1} M_\odot$) which is shown as the thin solid line in the bottom panel of Fig. 12 . The good agreement between WF2 and WF2LR indicates that numerical resolution effects are unlikely to compromise our conclusions.

According to the definition above, about 45% of WF2 galaxies are reasonably quiescent star-forming disks, and only about 20% are ongoing major mergers. These fractions are similar for WF2 and WF1, and seem consistent with the observational data quoted above.

For the run without feedback, NoF, over $\sim 75\%$ of the galaxies are classified as disks. This is because, in the absence of feedback, the gas cools and flows unimpeded to the center, where it settles into disks and forms stars profusely. These disks are, however, quite small (see Fig. 9). The absence of effective feedback allows the gas to remain undisturbed in such disks, which are quickly reconstituted after mergers (see, e.g., Springel & Hernquist 2005; Robertson et al. 2006). At the other extreme, only 5% of all galaxies in the AGN run, and $\sim 20\%$ of those in the WF2Dec run, would be classified as disks according to this criterion.

Strong feedback-driven winds can clearly disturb quiescent disk morphologies, and their kinematic effects may be difficult to disentangle from those of ongoing mergers. It remains to be seen whether a simple feedback model can account for both the observed frequency of galaxies with disk-like kinematics as well as the mounting evidence for large scale galactic outflows at $z \sim 2$ (Steidel et al. 2010).

5 SUMMARY AND CONCLUSIONS

We study the effects of various feedback implementations on the structure and morphology of simulated galaxies at $z = 2$. Our analysis uses nine runs from the OverWhelmingly Large Simulations (OWLS) project, and probe a variety of possible feedback implementations, from "no feedback" to supernova-driven wind feedback to strong outflows aided by the contribution from AGNs. Except for the no-feedback and AGN-feedback cases, all other runs assume that the *same amount* of feedback energy (per mass of stars formed) is devolved by supernovae to the interstellar medium: the main difference is *how* this energy is coupled to the medium, which in turn determines the overall effectiveness of the feedback.

Each run follows the evolution of the *same* $25\,h^{-1}$ Mpc box up to $z = 2$, with 512^3 dark matter particles and 512^3 particles for the baryonic component. All other simulation parame-
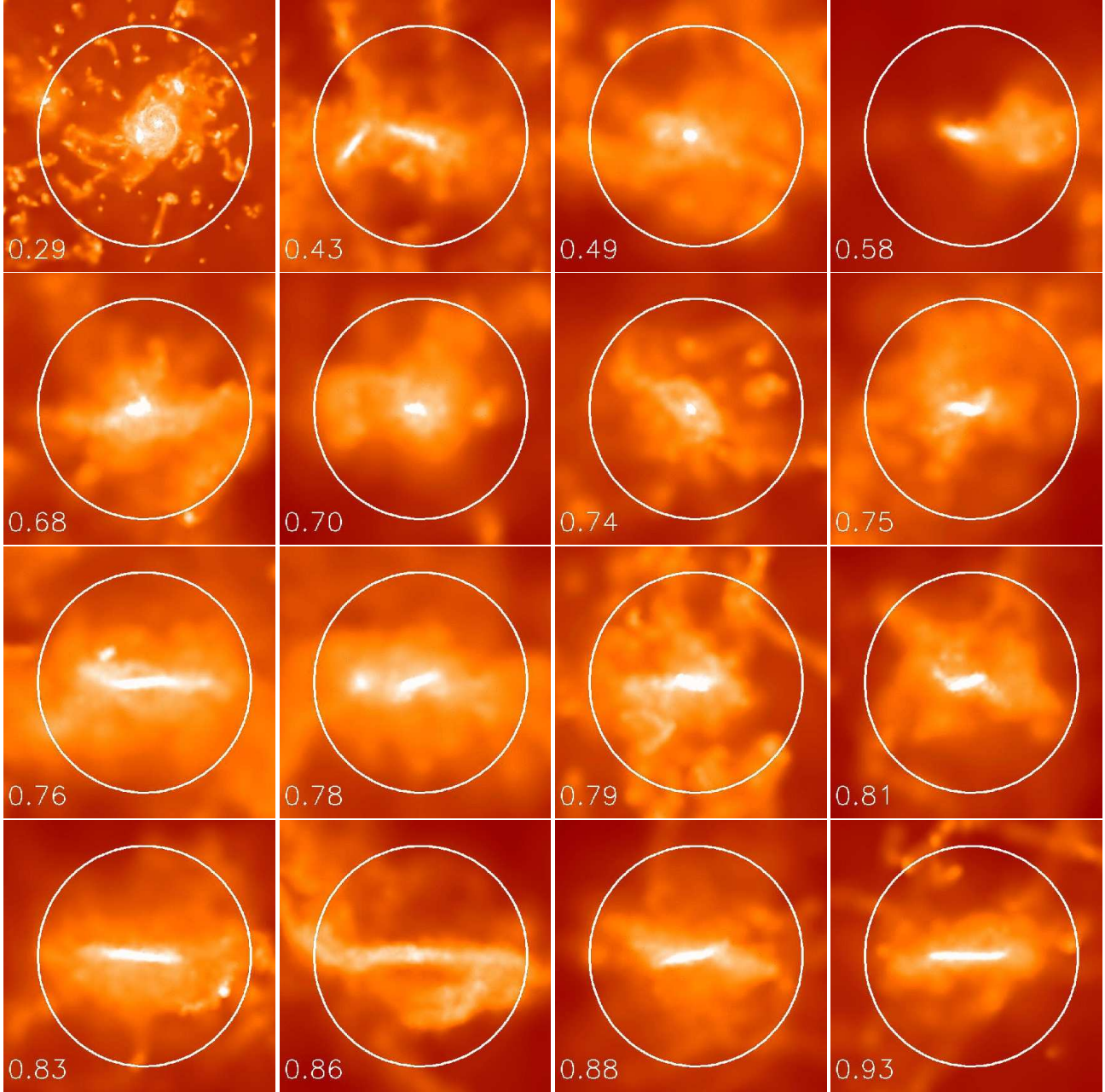
Figure 11. Edge-on view of galaxies spanning a wide range in rotational support taken from the WF2 run. Each panel is labelled by the value of $\kappa_{\rm rot}$ of the star-forming gas. Colors are assigned according to the (projected) logarithmic densities of the gas. Well-defined disk systems are apparent when $\kappa_{\rm rot} \gtrsim 0.75$; lower values of this parameter indicate ongoing mergers and/or systems with disturbed morphology. Solid circles indicate the region selected as the galaxy radii: $r_{\rm gal} = 0.15\, r_{\rm vir}$.

ters (star formation algorithm, stellar initial mass function, etc) are kept constant, so any differences between runs may be traced solely to feedback. In total, we analyze for each run ~ 150 galaxies formed at the centers of haloes with virial mass in the range $10^{11}\, h^{-1}\, M_\odot < M_{\rm vir} < 3 \times 10^{12} h^{-1} M_\odot$. Our main results may be summarized as follows.

• Varying the feedback implementation can lead to dramatic differences in the mass of galaxies formed in a given dark matter halo. The galaxy formation efficiency, $\eta_{\rm gal} = M_{\rm gal}/(f_{\rm bar} M_{\rm vir})$, varies by roughly an order of magnitude when comparing the no-feedback run (NoF, where $\eta_{\rm gal} \sim 0.5$) to the AGN+supernova feedback run

(AGN, where $\eta_{\rm gal} \sim 0.05$), the two extremes probed by our simulations.

• The ability of feedback to regulate the efficiency of galaxy formation in haloes of different mass varies according to the details of the adopted numerical implementation of the feedback. Weak or ineffective feedback leads to a decrease in galaxy formation efficiency with mass, whereas strong feedback curtails preferentially the formation of galaxies in low-mass haloes. The mass dependence is, however, modest, with variations in $\eta_{\rm gal}$ of less than a factor of ~ 2 over the (factor of ~ 30) mass range spanned by haloes in our sample.

• Feedback results in strong correlations between galaxy mass

and angular momentum. This leaves an imprint on galaxy morphologies and on the scaling laws relating mass, size, and circular velocity.

• Weak feedback minimizes disturbances to the settling of gas in rotationally-supported structures, and favors the formation and survival of quiescent *gaseous* disks. However, weak feedback also allows much of the gas to form stars early in dense protogalactic clumps that are later disrupted in mergers as the final galaxy assembles. Such mergers also transfer angular momentum from the baryons to the halo. The net result is a predominance of dense, spheroid-dominated stellar components and a scarcity of spatially-extended star-forming disks.

• Strong feedback, on the other hand, promotes the formation of large, extended galaxies. Indeed, the more efficient the feedback the more massive (and therefore, larger) the halo inhabited by a galaxy of given stellar mass. It is thus possible to have fairly large galaxies of modest stellar mass because, when feedback is strong, they inhabit large, massive haloes. The size, mass, and rotation speeds of these extended galaxies compare favorably with those reported by the SINS survey. This, however, comes at the expense of inhibiting the survival of rotationally-supported disks of quiescent kinematics and of preventing the formation of compact stellar spheroids.

• Moderate-feedback runs result in galaxies that follow scaling laws that are intermediate between large star-forming disks, such as those studied by the SINS collaboration (Förster Schreiber et al. 2009), and the compact, quiescent early-type systems analyzed by van Dokkum et al. (2008). Disk-like morphologies in both gas and stars are common in these runs, in numbers that appear commensurate with current constraints.

Although far from definitive, the results outlined above are encouraging. Properly calibrated, simple feedback recipes such as the ones we explore here seem able to produce galaxies with properties in broad agreement with observation. One should be aware, however, of the numerical sensitivity of the results to details of feedback implementation. Nevertheless, if developed in step with observational progress in the characterization of the high-redshift galaxy population, simulations are likely to become more and more reliable tools, useful when trying to make sense of the striking diversity of high-z galaxies in terms of the current paradigm of structure formation.

ACKNOWLEDGEMENTS

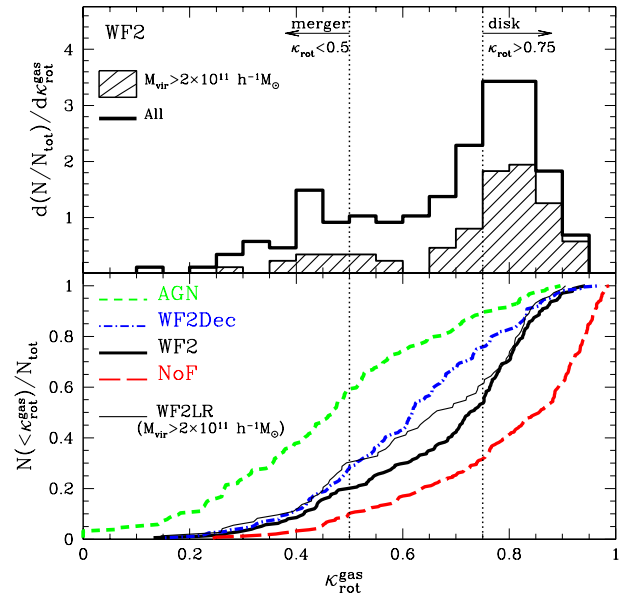**Figure 12.** Upper panel shows the histogram of $\kappa_{\rm rot} = K_{\rm rot}/K$, the fraction of kinetic energy of star-forming gas particles in ordered rotation for all galaxies in the WF2 run. The shaded red histogram is the same, but only for the half most massive, and therefore best numerically resolved, systems. The similarity between the two suggests that numerical resolution does not play a significant role in the statistics. $\kappa_{\rm rot}$ should be approximately unity for a disk where all particles are in circular orbits and much smaller for systems where ordered rotation plays a less important role. The large number of systems around $\kappa_{\rm rot} \sim 0.8$ indicates that systems where star formation occurs in well-defined disks are quite common in this run (see Fig. 11 for examples). The cumulative fraction of systems as a fraction of $\kappa_{\rm rot}$ for the four different feedback implementations are shown in the bottom panel. A trend for gaseous disks becoming more prevalent as feedback efficiency decreases is clearly seen.

REFERENCES

Abadi M. G., Navarro J. F., Steinmetz M., Eke V. R., 2003a, ApJ, 591, 499
Abadi M. G., Navarro J. F., Steinmetz M., Eke V. R., 2003b, ApJ, 597, 21
Bell E. F., de Jong R. S., 2001, ApJ, 550, 212
Birnboim Y., Dekel A., Neistein E., 2007, MNRAS, 380, 339
Blumenthal G. R., Faber S. M., Primack J. R., Rees M. J., 1985, Nature, 313, 72
Booth C. M., Schaye J., 2009, MNRAS, 398, 53
Brooks A. M., Governato F., Quinn T., Brook C. B., Wadsley J., 2009, ApJ, 694, 396
Bryan G. L., Norman M. L., 1998, ApJ, 495, 80
Chabrier G., 2003, ApJL, 586, L133
Cole S., 1991, ApJ, 367, 45
Cole S., Lacey C. G., Baugh C. M., Frenk C. S., 2000, MNRAS, 319, 168
Conroy C., Wechsler R. H., 2009, ApJ, 696, 620
Crain R. A., Theuns T., Dalla Vecchia C., Eke V. R., Frenk C. S., Jenkins A., Kay S. T., Peacock J. A., Pearce F. R., Schaye J.,

Springel V., Thomas P. A., White S. D. M., Wiersma R. P. C., 2009, MNRAS, 399, 1773

Dalla Vecchia C., Schaye J., 2008, MNRAS, 387, 1431

Dekel A., Birnboim Y., 2006, MNRAS, 368, 2

Dolag K., Borgani S., Murante G., Springel V., 2009, MNRAS, 399, 497

Fall S. M., Efstathiou G., 1980, MNRAS, 193, 189

Förster Schreiber N. M., Genzel R., Bouché N., Cresci G., Davies R., Buschkamp P., Shapiro K., Tacconi L. J., Hicks E. K. S., Genel S., Shapley A. E., Erb D. K., Steidel C. C., Lutz D., Eisenhauer e. a., 2009, ApJ, 706, 1364

Governato F., Brook C., Mayer L., Brooks A., Rhee G., Wadsley J., Jonsson P., Willman B., Stinson G., Quinn T., Madau P., 2010, Nature, 463, 203

Governato F., Willman B., Mayer L., Brooks A., Stinson G., Valenzuela O., Wadsley J., Quinn T., 2007, MNRAS, 374, 1479

Guo Q., White S., Li C., Boylan-Kolchin M., 2010, MNRAS, pp 367

Haardt F., Madau P., 2001, in D. M. Neumann & J. T. V. Tran ed., Clusters of Galaxies and the High Redshift Universe Observed in X-rays Modelling the UV/X-ray cosmic background with CUBA

Katz N., 1992, ApJ, 391, 502

Kay S. T., Thomas P. A., Theuns T., 2003, MNRAS, 343, 608

Kennicutt Jr. R. C., 1998, ARA&A, 36, 189

Kereš D., Katz N., Fardal M., Davé R., Weinberg D. H., 2009, MNRAS, 395, 160

Kereš D., Katz N., Weinberg D. H., Davé R., 2005, MNRAS, 363, 2

Law D. R., Steidel C. C., Erb D. K., Larkin J. E., Pettini M., Shapley A. E., Wright S. A., 2009, ApJ, 697, 2057

Li C., White S. D. M., 2009, MNRAS, 398, 2177

Marchesini D., van Dokkum P. G., Förster Schreiber N. M., Franx M., Labbé I., Wuyts S., 2009, ApJ, 701, 1765

McCarthy I. G., Schaye J., Ponman T. J., Bower R. G., Booth C. M., Dalla Vecchia C., Crain R. A., Springel V., Theuns T., Wiersma R. P. C., 2009, ArXiv:0911.2641

Meza A., Navarro J. F., Steinmetz M., Eke V. R., 2003, ApJ, 590, 619

Mo H. J., Mao S., White S. D. M., 1998, MNRAS, 295, 319

Navarro J. F., Benz W., 1991, ApJ, 380, 320

Navarro J. F., Frenk C. S., White S. D. M., 1995, MNRAS, 275, 56

Navarro J. F., Steinmetz M., 1997, ApJ, 478, 13

Okamoto T., Eke V. R., Frenk C. S., Jenkins A., 2005, MNRAS, 363, 1299

Robertson B., Bullock J. S., Cox T. J., Di Matteo T., Hernquist L., Springel V., Yoshida N., 2006, ApJ, 645, 986

Robertson B. E., Bullock J. S., 2008, ApJL, 685, L27

Sales L. V., Navarro J. F., Schaye J., Dalla Vecchia C., Springel V., Haas M. R., Helmi A., 2009, MNRAS, 399, L64

Scannapieco C., White S. D. M., Springel V., Tissera P. B., 2009, MNRAS, 396, 696

Schaye J., 2004, ApJ, 609, 667

Schaye J., Dalla Vecchia C., 2008, MNRAS, 383, 1210

Schaye J., Dalla Vecchia C., Booth C. M., Wiersma R. P. C., Theuns T., Haas M. R., Bertone S., Duffy A. R., McCarthy I. G., van de Voort F., 2010, MNRAS, 402, 1536

Springel V., Hernquist L., 2003, MNRAS, 339, 289

Springel V., Hernquist L., 2005, ApJL, 622, L9

Springel V., Yoshida N., White S. D. M., 2001, New Astronomy, 6, 79

Steidel C. C., Erb D. K., Shapley A. E., Pettini M., Reddy N. A., Bogosavljević M., Rudie G. C., Rakic O., 2010, ArXiv:1003.0679

Steinmetz M., Navarro J. F., 2002, New Astronomy, 7, 155

Toomre A., 1977, in Tinsley B. M., Larson R. B., eds, Evolution of Galaxies and Stellar Populations Mergers and Some Consequences. p. 401

van Dokkum P. G., Franx M., Kriek M., Holden B., Illingworth G. D., Magee D., Bouwens R., Marchesini D., Quadri R., Rudnick G., Taylor E. N., Toft S., 2008, ApJL, 677, L5

van Dokkum P. G., Kriek M., Franx M., 2009, Nature, 460, 717

White S. D. M., Frenk C. S., 1991, ApJ, 379, 52

White S. D. M., Rees M. J., 1978, MNRAS, 183, 341

Wiersma R. P. C., Schaye J., Smith B. D., 2009a, MNRAS, 393, 99

Wiersma R. P. C., Schaye J., Theuns T., Dalla Vecchia C., Tornatore L., 2009b, MNRAS, 399, 574

Yang X., Mo H. J., Jing Y. P., van den Bosch F. C., 2005, MNRAS, 358, 217

Zavala J., Okamoto T., Frenk C. S., 2008, MNRAS, 387, 364